Biophysical Journal
Article

Biophysical Society

The volume of healthy red blood cells is optimal for advective oxygen transport in arterioles

Lucas Amoudruz,[1] Athena Economides,[2] and Petros Koumoutsakos[1,*]
[1]Computational Science and Engineering Laboratory, School of Engineering and Applied Sciences, Harvard University, Cambridge, Massachusetts and [2]Institute of Neuropathology, University of Zurich, 8091 Zurich, Switzerland

ABSTRACT Red blood cells (RBCs) are vital for transporting oxygen from the lungs to the body's tissues through the intricate circulatory system. They achieve this by binding and releasing oxygen molecules to the abundant hemoglobin within their cytosol. The volume of RBCs affects the amount of oxygen they can carry, yet whether this volume is optimal for transporting oxygen through the circulatory system remains an open question. This study explores, through high-fidelity numerical simulations, the impact of RBC volume on advective oxygen transport efficiency through arterioles, which form the area of greatest flow resistance in the circulatory system. The results show that, strikingly, RBCs with volumes similar to those found in vivo are most efficient to transport oxygen through arterioles. The flow resistance is related to the cell-free layer thickness, which is influenced by the shape and the motion of the RBCs: at low volumes, RBCs deform and fold, while at high volumes, RBCs collide and follow more diffuse trajectories. In contrast, RBCs with a healthy volume maximize the cell-free layer thickness, resulting in a more efficient advective transport of oxygen.

SIGNIFICANCE The circulatory system plays a crucial role by delivering oxygen and essential nutrients to the body's tissues. This oxygen is transported by red blood cells (RBCs), which are the most abundant blood cells. The shape of these cells is influenced by both their membrane's mechanical characteristics and their volume, which, in turn, dictates their oxygen-carrying capacity. This study focuses on examining the impact of this volume on the efficiency of oxygen transport through arterioles, which contribute most to the flow resistance across the circulatory system. Our findings reveal that in these regions, the volume of healthy RBCs is the most effective for transporting oxygen.

INTRODUCTION

Blood flow plays a vital role in sustaining life, as it enables the delivery of oxygen and nutrients to every tissue and organ in the body while also removing harmful waste like carbon dioxide. Red blood cells (RBCs) are a crucial component of blood, making up almost half of the total blood volume in humans (1). These specialized cells are responsible for carrying oxygen from the lungs to the rest of the body, where it is used to fuel cellular metabolism. They are formed by a visco-elastic membrane that surrounds the cytosol of the cell. The cytosol contains a high concentration of hemoglobin, which is responsible for the transportation of oxygen (1,2). The RBC membrane is composed of a lipid bilayer anchored to a cytoskeleton and allows for significant deformations (3). The lipid bilayer of the membrane behaves like an incompressible liquid crystal with localized bending resistance, while the cytoskeleton provides resistance to local shear and dilation (4). According to current models, the unstressed shape of the cytoskeleton is an oblate spheroid of a reduced volume of approximately 0.95, compared to a sphere with the same membrane area (3–5). However, at equilibrium, healthy RBCs adopt a biconcave shape with a reduced volume (v) of approximately 0.65 (6). In this article, we study the effect of this reduced volume on the oxygen transport efficiency in straight tubes with a circular cross section that have representative characteristics of arterioles.

The biconcave shape and reduced volume of RBCs as well as metrics for their optimality remain a subject of debate in the scientific community. Several researchers proposed that the biconcave shape allows for a large surface/volume ratio for RBCs so that they maximize oxygen exchange between the RBC interior and their environment (7,8). The exchange of oxygen between the cytoplasm and the environment is higher for cells with lower thickness

Submitted October 23, 2023, and accepted for publication April 15, 2024.
*Correspondence: petros@seas.harvard.edu
Editor: Stephen Hall.
https://doi.org/10.1016/j.bpj.2024.04.015
© 2024 Biophysical Society.

because cytoplasmic diffusion may be more limiting than membrane permeability, as shown by Richardson et al. (9). Other studies suggest that the biconcave shape allows for a more efficient flow through capillaries and kidney tubules due to the RBCs' deformability (3,10–12). Uzoigwe (8) proposed that RBCs have a biconcave shape to maximize their moment of inertia, thereby reducing shear stresses in blood flow and decreasing blood flow resistance in arteries, but did not present any quantitative results. Guo et al. (13) showed that the volume of cells affects their stiffness, while other studies found that osmotic pressure and cell stiffness affect the viscosity of whole blood (14–17). Alterations in RBC volume can significantly impact the function of the circulatory system and individual health (8). Farutin et al. (18) studied numerically the cell transport efficiency in channels and observed that the optimal hematocrit depends on the RBCs' volume.

In this study, we investigate the effect of the reduced volume of RBCs on the advective oxygen transport efficiency along the blood flow direction. To this end, we study the transport of a fixed quantity of hemoglobin by RBCs with various resting shapes, parameterized by the reduced volume of the cells. We investigate the effect of the RBCs' reduced volume on the oxygen flux through a straight tube with a circular cross section. This metric has been used experimentally to determine the optimal hematocrit for oxygen transport (15,18). We chose tubes with dimensions and pressure gradients similar to those found in arterioles, where the flow resistance is the highest in the circulatory system (19–22).

The study relies on a recent and appropriately validated RBC model, comprising visco-elastic membranes enclosing the cytosol and suspended in the blood plasma. The model was extensively calibrated in Amoudruz et al. (5) and validated against experimental data in various flow conditions. The evolution of the solvent and the cytosol are described by dissipative particle dynamics (DPD) (23,24). The numerical simulations are performed with *Mirheo*, a high-performance software for blood flow and microfluidics (25).

MATERIALS AND METHODS

We model blood with RBCs composed of visco-elastic membranes surrounding their viscous cytosol and suspended in blood plasma. The RBC membrane deforms from forces that arise from bending resistance of the lipid bilayer, as well as due to the shear and dilation elasticity of the cytoskeleton with respect to its stress-free state (SFS) and membrane viscosity. The resistance to bending is described by the energy

$$U_{bending} = 2\kappa_b \oint H^2 dA, \qquad \text{(Equation 1)}$$

where the integral is taken over the membrane surface, κ_b is the bending modulus, and H is the local mean curvature. The in-plane elastic energy is given by

$$U_{in-plane} = \frac{K_\alpha}{2}\oint\left(\alpha^2 + a_3\alpha^3 + a_4\alpha^4\right)dA_0 + \mu\oint\left(\beta + b_1\alpha\beta + b_2\beta^2\right)dA_0, \qquad \text{(Equation 2)}$$

where the integral is taken over the SFS surface; α and β are the local dilation and shear strain invariants, respectively; K_α is the dilation elastic modulus; μ is the shear elastic modulus; and the coefficients a_3, a_4, b_1, and b_2 are parameters that control the nonlinearity of the membrane elasticity for large deformations (26).

Each membrane is composed of 2562 particles located at the corners of a triangulated mesh and evolve according to Newton's law of motion. The bending energy is discretized following (27,28), and the in-plane energy is computed as described in Lim et al. (3). The forces acting on the particles are the negative gradients of the discretized energy terms, with respect to the particle positions. Dissipation on the membrane is modeled by particles sharing an edge in the triangle mesh that exert a pairwise force as described in Fedosov (29), proportional to the membrane viscosity η_m. Finally, the area of the membrane and the volume of the cytosol are constrained through energy penalization terms

$$U_{area} = k_A\frac{(A - A_0)^2}{A_0} \quad \text{and} \quad U_{volume} = k_V\frac{(V - V_0)^2}{V_0}, \qquad \text{(Equation 3)}$$

where A_0 and V_0 are the area and volume of the cell at rest and A and V are the area and volume of the cell, respectively. These penalization terms are required, as the DPD method does not impose incompressibility of the cytosol, and the membrane elastic energies alone do not conserve the membrane area. The parameters of the model take physiological values calibrated from experimental data (5) and are listed in the appendix.

The RBC cytosol and surrounding plasma are represented with particles that evolve through DPD interactions (5,23,24) (see the appendix for more details). We emphasize that the model parameters correspond to the 1:5 ratio of viscosities for the plasma (1.2 Pa s (30)) and the RBC cytosol (6 Pa s (31)). To model the no-slip and no-flux boundary conditions on walls, particles are bounced back from the walls' surface. Furthermore, the particles interact with a layer of frozen particles that are inside the walls through DPD interactions (32). In addition, DPD particles are bounced back from membrane surfaces and interact with the membrane particles through the dissipative and stochastic parts of the DPD interactions only (29). The cytosol and plasma particles interact with each other only through the conservative part of the DPD forces. The DPD parameters are chosen from the macroscopic properties of the fluids as described in (33).

RESULTS

We examine the equilibrated flow of RBCs inside a circular tube of radius $R \in \{30\ \mu\text{m}, 40\ \mu\text{m}\}$. These sizes are typical for arterioles (34). The volume fraction of RBCs, or tube hematocrit, is set to $\text{Hct} \in \{40\%, 45\%, 50\%\}$, and the blood suspension is subjected to a pressure gradient $\nabla p \in \{1 \times 10^{-3}\text{cmH}_2\text{O}\ \mu\text{m}^{-1}, 2 \times 10^{-3}\text{cmH}_2\text{O}\ \mu\text{m}^{-1}\}$, typical for arterioles of this size (34). These conditions correspond to mean flow velocities of the order of 10 mm s^{-1}, consistent with values reported in the literature (1). Mean flow velocities of all simulations are reported in Fig. 1. We study different cases where all RBC membranes have the same area and visco-elastic properties (calibrated from experimental data (5)) but have a different volume V_0

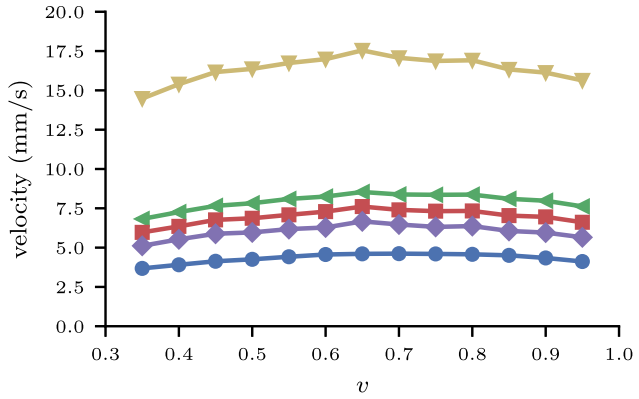

FIGURE 1 Mean flow velocity in the tube against the reduced volume of the RBCs for a fixed pressure gradient, with different tube radii, hematocrits and pressure gradients. Line with circles: $R = 30$ μm, Hct = 40%, $\nabla p = 1 \times 10^{-3}$ cm H_20 μm^{-1}; line with left-facing triangles: $R = 40$ μm, Hct = 40%, $\nabla p = 1 \times 10^{-3}$ cm H_20 μm^{-1}; line with squares: $R = 40$ μm, Hct = 45%, $\nabla p = 1 \times 10^{-3}$ cm H_20 μm^{-1}; line with diamonds: $R = 40$ μm, Hct = 50%, $\nabla p = 1 \times 10^{-3}$ cm H_20 μm^{-1}; and line with inverse triangles: $R = 40$ μm, Hct = 45%, $\nabla p = 2 \times 10^{-3}$ cm H_20 μm^{-1}. To see this figure in color, go online.

parameterized by the reduced volume $v = V_0/V_s$, where V_s is the volume of a sphere with the same area as the cell's membrane. All initial triangle meshes were produced by minimizing the membrane energy with a target volume V_0. The number of RBCs is adapted to keep the hematocrit constant, $N = \lfloor \pi R^2 L \mathrm{Hct}/V_0 \rfloor$. We study a periodic domain with a length $L = 100$ μm along the flow direction. No-slip and no-flux boundary conditions are applied on the side walls. All quantities are reported from equilibrated blood flows.

We find that the reduced volume affects the flow patterns and RBCs' deformability (Fig. 2). Specifically, for low reduced volumes, the cells deform much more than at high values of v. In the limit $v \to 1$, only spherical cells are allowed, and as the area is constant, they cannot deform. RBCs with a physiological reduced volume do not exhibit significant deformations compared to those with lower reduced volumes. Instead, RBCs with $v = 0.65$ seem to keep a relatively flat shape similar to tank-treading RBCs, a type of motion where the membrane rotates around a steady elongated shape similar to tank treads (35).

We quantify the amount of transported oxygen by computing the flux of cytosol in the tube for each value of v,

$$Q_c = \frac{V_0}{L} \sum_{i=1}^{N} U_i, \qquad \text{(Equation 4)}$$

where U_i is the time-averaged velocity of the i^{th} RBC's center of mass. We assume that the hemoglobin concentration inside the cytosol is constant and therefore the cytosol flux is proportional to the oxygen flux. Fig. 3 shows the flux of cytosol against the reduced volume of the RBCs for different tube radii and hematocrits. The flux of cytosol is normalized by the flux of plasma with no RBCs, $Q_p = |\nabla p| \pi R^4 / 8\eta$, where η is the dynamic viscosity of the plasma. In these conditions, Q_c reaches a maximum at a reduced volume $v \approx 0.65$. Strikingly, the oxygen flux is maximized at the physiological reduced volume of RBCs.

To elucidate the mechanisms that reduce the cytosol flux when the volume of the RBCs deviates from its physiological value, we examine the cell-free layer (CFL) near the walls of the tube (Fig. 4). We report its thickness, δ, with respect to the reduced volume v in Fig. 5. The viscosity is lower in the CFL than in the blood suspension, hence the shear rate is higher in the CFL region. Therefore, for a given pressure difference, a larger CFL thickness causes a higher flux of hemoglobin (Figs. 3 and 5) (36). We suggest that the change in the CFL thickness depends on the reduced volume of the RBCs. It has been reported in the literature that cells that are close to the walls in a Poiseuille flow tend to migrate toward the center of the pipe due to their deformability (37). In contrast, a large volume fraction of RBCs may cause the cells to move closer to the walls due to collisions between the cells. In the remainder of this study, we investigate the deformations of RBCs and their trajectories and correlate these observations to the CFL thickness. The deformation of the cells is quantified by the rim angle (see below) and the bending energy of each cell. We distinguish tumbling-like motion, due to the external shear stresses, from tank-treading motion, where the membrane rotates around a steady shape. The cell trajectories are quantified by the diffusion coefficient along the radial direction. We fix

FIGURE 2 Snapshots of RBCs flowing near the walls of the tube with $R = 40$ μm and Hct $= 0.45$. The flow direction is from left to right. Cells with different reduced volumes respond differently to the flow shear (from *left to right*: $v = 0.35, 0.65, 0.95$). To see this figure in color, go online.

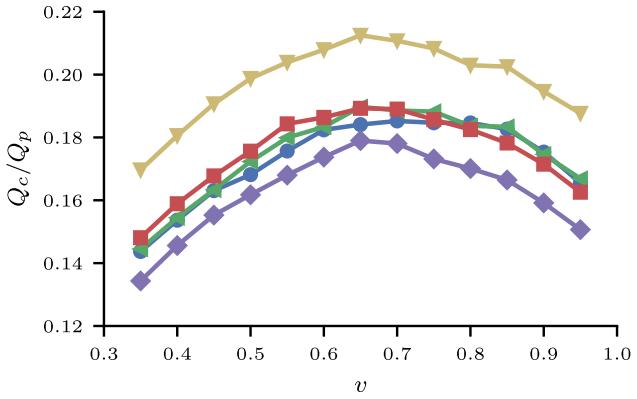

FIGURE 3 Cytosol flux Q_c, normalized by that of the plasma at zero hematocrit, Q_p, against the reduced volume of RBCs v flowing in the tube of different radii and hematocrits. Same labels as in Fig. 1. To see this figure in color, go online.

$R = 40\ \mu$m, $\nabla p = 1 \times 10^{-3}cmH_2$O μm^{-1}, and Hct = 0.45 for clarity, but similar results were observed for the other conditions listed in Fig. 1.

Rim angle

In a sufficiently high shear, the RBC membrane rotates around the cytosol (35). In this situation, the region of the membrane that forms the rim at equilibrium differs from the principal disc of the deformed cell, unlike RBCs at rest. We define the rim angle as the angle between the normal to the principal disc of the cell and the normal to the region corresponding to the rim of the SFS of the cell (see Fig. 6 and (38)). For a tumbling RBC, this angle is typically low, while for tank-treading RBCs, the angle takes values in the whole range, $\theta \in [0, \pi/2]$. Fig. 6 shows the distribution of rim angles θ of cells flowing in the tube for different values of v. On average, the rim angles are smaller at low values of v. Furthermore, the density of θ is more uniform at high values of v than at low reduced volume values. This suggests that RBCs with a large reduced volume tank tread, while their motion is closer to tumbling at lower values of v.

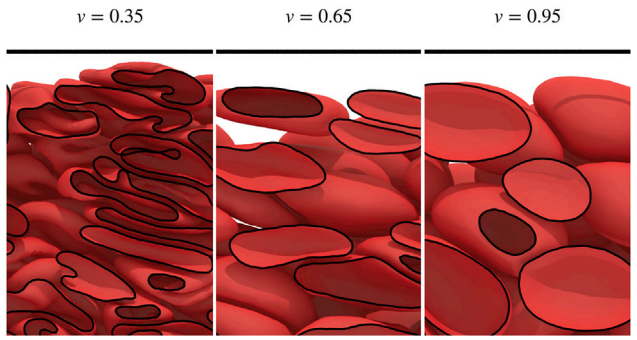

FIGURE 4 Snapshots of RBCs flowing near the walls (top horizontal line) of the tube. The flow direction is from left to right. The slice of the RBCs in the vertical plane is represented with black lines. To see this figure in color, go online.

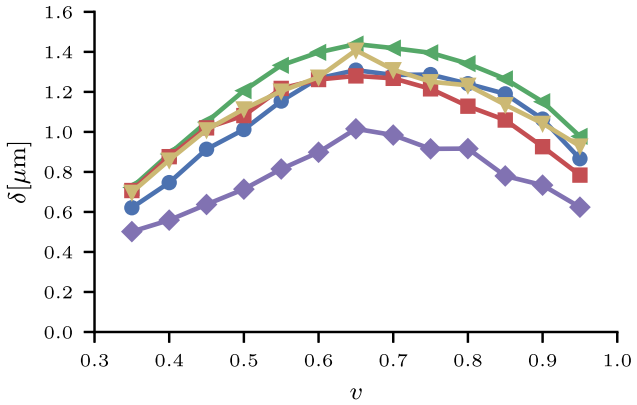

FIGURE 5 Cell-free layer thickness δ against the reduced volume of RBCs v flowing in the tube. Same labels as in Fig. 1. To see this figure in color, go online.

Bending energy

The deformations of the cells are characterized by the bending energy described by Eq. 1. This energy is high when the cell deforms (e.g., folds) and therefore characterizes complex dynamics and shape changes. The bending energy distribution of the cells is shown in Fig. 7 for different values of v. The mean bending energy decreases when v increases, consistent with the fact that the minimum bending energy is achieved for a spherical shape. Nevertheless, we observe differences in the distributions of the bending energies. For $v \geq 0.6$, the bending energies are concentrated close to a minimal value. Instead, when $v < 0.6$, we observe a peak of bending energy well above the minimal values observed at each reduced volume. These high values suggest that RBCs undergo large deformations compared to their resting shape. In particular, we observe cells that are "folding" periodically when v is relatively small (Fig. 7), as opposed to cells that have a large reduced volume. These large deformations cause a large bending energy density in the bulk or, equivalently, a large pressure compared to configurations with undeformed cells. The larger deformations

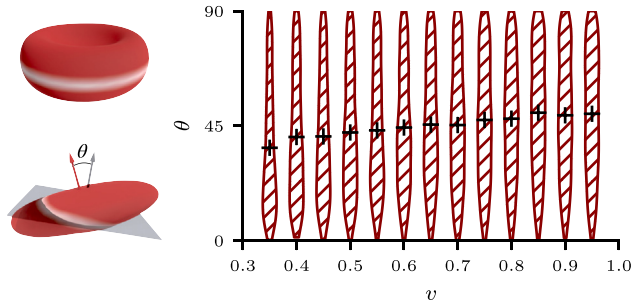

FIGURE 6 Top left: the rim (*white*) of an RBC at rest. Bottom left: the normal of the rim plane (*right arrow*) and the normal of the cell plane (*left arrow*) form the rim angle θ. Right: violin plots illustrating the variation in rim angle distribution θ (in degrees) of flowing cells across different reduced volumes v. Crosses indicate the mean value of θ. To see this figure in color, go online.

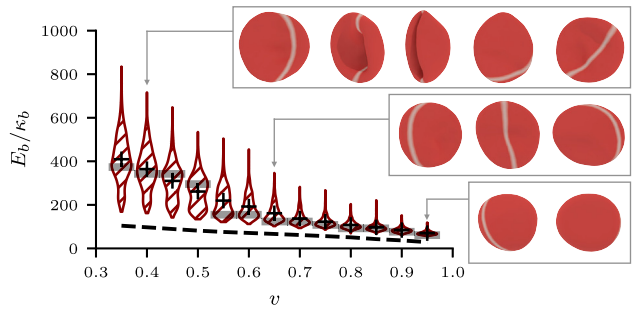

FIGURE 7 Left: violin plots illustrating the variation in bending energy distribution of flowing cells across different reduced volumes v. Crosses indicate the mean value of the bending energy, and shaded regions indicate the maximum density. The dashed line corresponds to the bending energy of the cells at rest. κ_b is the bending modulus. Right: time sequences of typical RBCs in the tube (time increasing from *left to right*). From top to bottom: $v = 0.4$, $v = 0.65$, and $v = 0.95$. The white stripe represents the rim of the cell at rest (see Fig. 6). To see this figure in color, go online.

associated with low reduced volumes may thus contribute to reducing the CFL thickness in this regime. Furthermore, the deformation of RBCs is accompanied by an additional dissipation due to the membrane viscosity and the recirculation of the cytosol inside the cell (35), which may further decrease the blood flux.

TTF

In linear shear flows, RBCs tank tread when the shear rate is large enough (39,40). The tank-treading frequency (TTF) is reported against the time-averaged radial position of the cells in Fig. 8 (see the appendix for details). For low values of v, most cells do not tank tread, hence the value estimated for the TTF is low. For larger values of v, the TTF increases linearly with the radial position. This increase is consistent with the nearly linear relationship between the TTF and the shear rate for single cells (39), and assuming that we have a nearly parabolic velocity profile along the radial direction of the tube, hence a linear increase of the shear rate with the radial position r. Furthermore, we observe that the TTF of cells is larger when v increases. This is also expected since spheres in shear flows rotate with a larger frequency than the TTF of RBCs (39). We suggest that, for relatively thin cells,

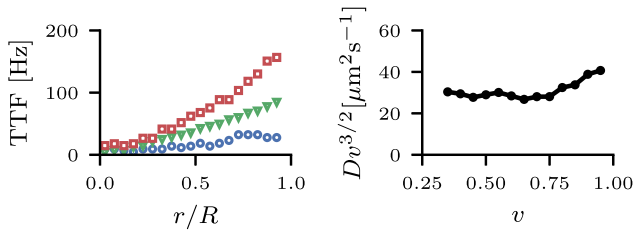

FIGURE 8 Left: TTF of the RBCs against their time-averaged radial position for $v = 0.4$ (*circles*), $v = 0.7$ (*triangles*), and $v = 0.9$ (*squares*). Right: radial diffusion D of the RBCs against the reduced volume v. To see this figure in color, go online.

tank treading is beneficial for cells to pass each other without deforming and to minimize the effect of their collisions, thus contributing to a lower value of δ. It was shown that tank-treading provides less hindrance to the motion of other particles compared to other motions like tumbling (41). This may be an indication that tank-treading cells contribute to a lower value of δ compared to other motions, present notably at low values of v.

Radial diffusion

RBCs in blood flow undergo shear-induced diffusion, which is a result of the cell-cell interactions. These interactions influence the radial distribution of the cells and the CFL thickness (42,43). We thus measure the radial diffusion coefficient of the RBCs in the tube. The diffusion coefficient is estimated from the mean-squared displacement of the cells along the radial direction:

$$D = \langle (r(T) - r(0))^2 \rangle / 2T, \qquad \text{(Equation 5)}$$

where r is the radial position of the cell's center of mass and T is a time large enough to collect statistics but small enough to remain in the linear regime of the mean-squared displacement against time.

The theory of shear-induced diffusion suggests that, at a given volume fraction, $D \propto \dot{\gamma} a^2$, where $\dot{\gamma}$ is the shear rate and a is the size of the particle (44). Assuming that the shear rate is constant across the simulations and $a \propto v^{1/3}$, we expect $Dv^{3/2}$ to be approximately constant against v. This quantity is reported in Fig. 8. We observe that $Dv^{3/2}$ remains constant within a 30% deviation, suggesting that increasing v increases the shear-induced diffusion. The deviations from the theory may come from the cells' deformability, the definition of the cell radius from v, or the nonconstant shear rate along the radial direction. The shear-induced diffusion is higher for larger values of v and may thus contribute to reducing the CFL thickness for $v > 0.65$ (43), hence decreasing the transport efficiency of the cytosol.

DISCUSSION

The physiological volume of RBCs, under the assumptions made in this study, is the most efficient to transport oxygen through tubes that have the characteristics of arterioles. When the reduced volume of the RBCs deviates from its physiological value, we identify two factors that decrease the transport efficiency of oxygen: the change of the CFL thickness and the dissipation due to the cytosol recirculation and the deformations of the cells.

The viscosity of plasma is smaller than that of whole blood, thus a larger CFL thickness contributes to a higher flux of blood. We find that the CFL thickness is maximized at $v \approx 0.65$. Below this value, cells fold, undergo large deformations, and adopt a tumbling rather than tank-treading

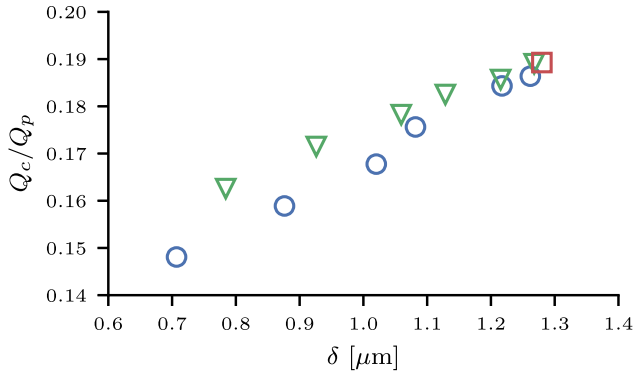

FIGURE 9 Cytosol flux against the CFL thickness. Circles correspond to cells with $v < 0.65$, triangles those with $v > 0.65$, and the square is for $v = 0.65$. To see this figure in color, go online.

motion. These deformations increase the effective thickness of the cells along the radial direction, thus reducing the CFL thickness. In contrast, at larger values of v, cells do not deform and have more diffusive trajectories due to collisions with their neighboring cells. These collisions cause the cells to migrate perpendicularly to the flow direction, thus reducing the CFL thickness. At intermediate values of v, the cells tank tread, which facilitates their motion relative to each other. This is supported by the shear-thinning behavior of blood when the motion of RBCs transitions from tumbling to tank treading (45,46). The nonspherical shape of RBCs limits the effect of collisions, and they form a maximal CFL thickness.

The CFL thickness alone does not explain the profile observed in Fig. 3. Indeed, for the same value of CFL thickness, the cytosol flux is lower for the case with $v < 0.65$ than when $v > 0.65$ (Fig. 9). We attribute this difference to the additional dissipation due to the large deformations occurring for cells with smaller reduced volumes, as membrane deformation was shown to be a dissipative process (47). In addition, we expect that tank-treading cells dissipate more energy at lower reduced volumes, as shown for vesicles (48).

In this study, we tackled the following question: what is the reduced volume that corresponds to the highest flux of a given amount of hemoglobin? We achieved this by adjusting the number of RBCs, assuming that the concentration of hemoglobin in the cytosol is the same in every situation. However, we could also consider a hemoglobin concentration that varies with v, e.g., a higher concentration at low values of v to model erythropoiesis (49), but this approach would require us to model the dependence of the cytosol viscosity with the hemoglobin concentration. These different concentrations would change the volume of oxygen transported by the system and the viscosity of the cytosol. In this study, we did not explore these effects due to the large computational cost of the simulations and made the approximation that the hemoglobin remains constant across all cases, which corresponds to the simplest model. We leave the more complex scenario of varying the concentration as well as the number of RBCs to further studies.

The results of this study are valid for straight tubes, which are a simplistic approximation of arterioles. The CFL thickness is known to vary around bifurcations (50–53) or curved geometries (54). However, the deformation of cells at low v and the collisions of cells at larger values of v might still contribute to reduce the CFL thickness in those conditions compared to the physiological values, and we thus expect the same trend as in straight tubes. Nevertheless, the optimal value of v might slightly differ in those cases, and further studies are required to provide a quantitative description of these variations.

Finally, we remark that we considered the advective part of oxygen transport in arterioles. The diffusive transport of oxygen, not studied in this work, is responsible for transporting oxygen across the RBC membranes. This type of transport may be affected by the shape, and thus the reduced volume, of RBCs (7–9).

CONCLUSION

We demonstrate, through high-fidelity simulations, that RBCs with volumes similar to those observed in vivo maximize the efficiency of advective oxygen transport in straight tubes that have characteristics of arterioles, where the vascular resistance is maximal. We qualitatively explain the variation of advective oxygen transport efficiency with respect to the reduced volume of the cells based on the CFL thickness and the dissipation due to the cells' deformability. At low reduced volumes, cells deform and fold, thus occupying a larger effective volume on average. This causes the CFL thickness to decrease. The deformations of cells induce additional dissipation due to the recirculation of the cytosol and the highly viscous membranes. At large reduced volumes, cells collide and migrate in the directions perpendicular to the flow due to a high shear-induced diffusion. These trajectories also contribute to reducing the CFL thickness, and thus the oxygen transport is lower.

The present findings provide valuable insights into the mechanisms of advective oxygen transport in the body and could potentially have significant implications for the advancement of therapies aimed at treating circulatory disorders.

APPENDIX

DPD

The DPD method discretizes a fluid into N particles with position $\mathbf{r}_i$, velocity $\mathbf{v}_i$, and mass m, $i = 1,2,\ldots,N$. The particles evolve according to Newton's law of motion,

$$\dot{\mathbf{r}}_i = \mathbf{v}_i, \quad \dot{\mathbf{v}}_i = \frac{1}{m}\sum_{j=1}^{N}\mathbf{F}_{ij},$$

TABLE 1 Parameters of the RBC model

Parameter	Value
κ_b	2.10×10^{-19} J
μ	4.99 μN m^{-1}
K_α	4.99 μN m^{-1}
a_3	$-$ 2
a_4	8
b_1	0.7
b_2	1.84
η_m	0.42×10^{-6} Pa s m
A_0	135 μm^2
V_0	varying
k_A	0.5 J/m^2
k_V	7.23×10^5 J/m^3

where $\mathbf{F}_{ij}$ are pairwise forces that vanish after a cutoff distance r_c. These interactions are formed by three terms (23,24),

$$\mathbf{F}_{ij} = aw(r_{ij})\mathbf{e}_{ij} - \gamma(\mathbf{e}_{ij}\cdot\mathbf{v}_{ij})w_D(r_{ij})\mathbf{e}_{ij} + \sigma\xi_{ij}w_R(r_{ij})\mathbf{e}_{ij},$$

where $\mathbf{v}_{ij} = \mathbf{v}_i - \mathbf{v}_j$, $\mathbf{r}_{ij} = \mathbf{r}_i - \mathbf{r}_j$, $r_{ij} = \|\mathbf{r}_{ij}\|$, and $\mathbf{e}_{ij} = \mathbf{r}_{ij}/r_{ij}$. The coefficients a, γ, and σ are the conservative, dissipative, and random force magnitudes, respectively. Furthermore, we use the standard DPD conservative kernel

$$w(r) = \begin{cases} 1 - r/r_c, & r < r_c, \\ 0, & \text{otherwise.} \end{cases}$$

We set $w_D = w^{1/4}$. w_R satisfies the fluctuation-dissipation theorem, $\sigma^2 = 2\gamma k_B T$ and $w_D = w_R^2$ (24), where $k_B T$ is the temperature of the system in energy units.

Parameters of the model

The values of the RBC parameters are listed in Table 1. They correspond to the mean value of the posterior distribution found in (5).

Computation of the CFL thickness

The CFL thickness δ is computed from the vertices of the RBC membranes. For a given time snapshot, we compute the maximum radial position of vertices over bins placed at regular intervals along the flow direction. The bins have a size of 1 μm. The value of δ at a given time is then the difference between the radius of the pipe and the average of this quantity over all bins. The values reported in this work are the average of the CFL thickness over time, after equilibration of the flow.

Computation of the TTF

The TTF is estimated by computing the Fourier transform of the rim angle time series of each cell and selecting the frequency of the largest mode, divided by 2, since the rim angle of a tank-treading cell undergoes 2 revolutions per tank-treading revolution. Note that we exclude cells having an average rim angle $\overline{\theta}$ larger than $\pi/4$ and the tumbling cells, which we characterize by $\overline{\theta} < \pi/8$.

AUTHOR CONTRIBUTIONS

L.A., A.E., and P.K. designed research. L.A. performed research. L.A. and A.E. analyzed data. L.A., A.E., and P.K. wrote the manuscript.

ACKNOWLEDGMENTS

We would like to thank Xin Bian for the idea of using the rim angle to perform the analysis. We acknowledge the computational resources granted by the Swiss National Supercomputing Center (CSCS) under the project ID "s1160."

DECLARATION OF INTERESTS

The authors declare no competing interests.

REFERENCES

1. Popel, A. S. 1989. Theory of oxygen transport to tissue. *Crit. Rev. Biomed. Eng.* 17:257–321.
2. Di Caprio, G., C. Stokes, …, E. Schonbrun. 2015. Single-cell measurement of red blood cell oxygen affinity. *Proc. Natl. Acad. Sci. USA.* 112:9984–9989.
3. Lim, H. W. ,G., M. Wortis, and R. Mukhopadhyay. 2008. Red Blood Cell Shapes and Shape Transformations: Newtonian Mechanics of a Composite Membrane. *Soft Matter.* 4:83–139.
4. Geekiyanage, N. M., M. A. Balanant, …, Y. Gu. 2019. A coarse-grained red blood cell membrane model to study stomatocyte-discocyte-echinocyte morphologies. *PLoS One.* 14, e0215447.
5. Amoudruz, L., A. Economides, …, P. Koumoutsakos. 2023. The stress-free state of human erythrocytes: Data-driven inference of a transferable RBC model. *Biophys. J.* 122:1517–1525.
6. Evans, E., and Y. C. Fung. 1972. Improved measurements of the erythrocyte geometry. *Microvasc. Res.* 4:335–347.
7. Lenard, J. G. 1974. A note on the shape of the erythrocyte. *Bull. Math. Biol.* 36:55–58.
8. Uzoigwe, C. 2006. The human erythrocyte has developed the biconcave disc shape to optimise the flow properties of the blood in the large vessels. *Med. Hypotheses.* 67:1159–1163.
9. Richardson, S. L., A. Hulikova, …, P. Swietach. 2020. Single-cell O_2 exchange imaging shows that cytoplasmic diffusion is a dominant barrier to efficient gas transport in red blood cells. *Proc. Natl. Acad. Sci. USA.* 117:10067–10078.
10. Pivkin, I. V., Z. Peng, …, S. Suresh. 2016. Biomechanics of red blood cells in human spleen and consequences for physiology and disease. *Proc. Natl. Acad. Sci. USA.* 113:7804–7809.
11. Vahidkhah, K., P. Balogh, and P. Bagchi. 2016. Flow of red blood cells in stenosed microvessels. *Sci. Rep.* 6:28194.
12. Namvar, A., A. J. Blanch, …, L. Tilley. 2021. Surface area-to-volume ratio, not cellular viscoelasticity, is the major determinant of red blood cell traversal through small channels. *Cell Microbiol.* 23, e13270.
13. Guo, M., A. F. Pegoraro, …, D. A. Weitz. 2017. Cell volume change through water efflux impacts cell stiffness and stem cell fate. *Proc. Natl. Acad. Sci. USA.* 114:E8618–E8627.
14. Strumia, M. M., M. Phillips, …, P. Mariano. 1963. Effect of red cell factors on the relative viscosity of whole blood. *Am. J. Clin. Pathol.* 39:464–474.
15. Stone, H. O., H. K. Thompson, Jr., and K. Schmidt-Nielsen. 1968. Influence of erythrocytes on blood viscosity. *Am. J. Physiol.* 214:913–918.
16. Reinhart, W. H., M. Singh-Marchetti, and P. W. Straub. 1992. The influence of erythrocyte shape on suspension viscosities. *Eur. J. Clin. Invest.* 22:38–44.
17. Schmid-Schönbein, H., and R. E. Wells, Jr. 1971. Rheological properties of human erythrocytes and their influence upon the "anomalous" viscosity of blood. *Ergeb. Physiol.* 63:146–219.
18. Farutin, A., Z. Shen, …, C. Misbah. 2018. Optimal cell transport in straight channels and networks. *Phys. Rev. Fluids.* 3, 103603.

19. Bohlen, H. G., R. W. Gore, and P. M. Hutchins. 1977. Comparison of microvascular pressures in normal and spontaneously hypertensive rats. *Microvasc. Res.* 13:125–130.
20. Chilian, W. M., C. L. Eastham, and M. L. Marcus. 1986. Microvascular distribution of coronary vascular resistance in beating left ventricle. *Am. J. Physiol.* 251:H779–H788.
21. Meininger, G. A. 1987. Responses of sequentially branching macro- and microvessels during reactive hyperemia in skeletal muscle. *Microvasc. Res.* 34:29–45.
22. Mulvany, M. J., and C. Aalkjaer. 1990. Structure and function of small arteries. *Physiol. Rev.* 70:921–961.
23. Hoogerbrugge, P. J., and J. M. V. A. Koelman. 1992. Simulating microscopic hydrodynamic phenomena with dissipative particle dynamics. *EPL.* 19:155–160.
24. Español, P., and P. Warren. 1995. Statistical mechanics of dissipative particle dynamics. *EPL.* 30:191–196.
25. Alexeev, D., L. Amoudruz, …, P. Koumoutsakos. 2020. Mirheo: High-performance mesoscale simulations for microfluidics. *Comput. Phys. Commun.* 254, 107298.
26. Lim H W, G., M. Wortis, and R. Mukhopadhyay. 2002. Stomatocyte–discocyte–echinocyte sequence of the human red blood cell: Evidence for the bilayer–couple hypothesis from membrane mechanics. *Proc. Natl. Acad. Sci. USA.* 99:16766–16769.
27. Jülicher, F. 1996. The morphology of vesicles of higher topological genus: conformal degeneracy and conformal modes. *J. Phys. II France.* 6:1797–1824.
28. Bian, X., S. Litvinov, and P. Koumoutsakos. 2020. Bending models of lipid bilayer membranes: Spontaneous curvature and area-difference elasticity. *Comput. Methods Appl. Math.* 359, 112758.
29. Fedosov, D. A. 2010. Multiscale Modeling of Blood Flow and Soft Matter, Ph.D. thesis. Citeseer.
30. Wells, R. E., and E. W. Merrill. 1961. Shear rate dependence of the viscosity of whole blood and plasma. *Science.* 133:763–764.
31. Wells, R., and H. Schmid-Schönbein. 1969. Red cell deformation and fluidity of concentrated cell suspensions. *J. Appl. Physiol.* 27:213–217.
32. Revenga, M., I. Zúñiga, …, I. Pagonabarraga. 1998. Boundary models in DPD. *Int. J. Mod. Phys. C.* 09:1319–1328.
33. Amoudruz, L. 2022. Simulations and Control of Artificial Microswimmers in Blood, Ph.D. thesis. ETH Zurich.
34. Fung, Y.-C. 1998. Biomechanics: circulation. *Shock.* 9:155.
35. Fischer, T. M. 1980. On the energy dissipation in a tank-treading human red blood cell. *Biophys. J.* 32:863–868.
36. Cokelet, G. R., and H. L. Goldsmith. 1991. Decreased hydrodynamic resistance in the two-phase flow of blood through small vertical tubes at low flow rates. *Circ. Res.* 68:1–17.
37. Shi, L., T.-W. Pan, and R. Glowinski. 2012. Numerical simulation of lateral migration of red blood cells in Poiseuille flows. *Int. J. Numer. Methods Fluid.* 68:1393–1408.
38. Economides, E. A. 2020. Data Informed, Predictive Simulations of Blood Microfluidics, Ph.D. thesis. ETH Zurich.
39. Fischer, T. M. 2007. Tank-Tread Frequency of the Red Cell Membrane : Dependence on the Viscosity of the Suspending Medium. *Biophys. J.* 93:2553–2561.
40. Dupire, J., M. Socol, and A. Viallat. 2012. Full dynamics of a red blood cell in shear flow. *Proc. Natl. Acad. Sci. USA.* 109:20808–20813.
41. Krüger, T., M. Gross, …, F. Varnik. 2013. Crossover from tumbling to tank-treading-like motion in dense simulated suspensions of red blood cells. *Soft Matter.* 9:9008–9015.
42. Higgins, J. M., D. T. Eddington, …, L. Mahadevan. 2009. Statistical dynamics of flowing red blood cells by morphological image processing. *PLoS Comput. Biol.* 5, e1000288.
43. Srivastav, A., X. Grandchamp, …, T. Podgorski. 2012. Shear-induced diffusion in a red blood cell suspension. *Comput. Methods Biomech. Biomed. Eng.* 15:34–35.
44. Rognon, P., and M. Macaulay. 2021. Shear-induced diffusion in dense granular fluids. *Soft Matter.* 17:5271–5277.
45. Fedosov, D. A., W. Pan, …, G. E. Karniadakis. 2011. Predicting human blood viscosity in silico. *Proc. Natl. Acad. Sci. USA.* 108:11772–11777.
46. Forsyth, A. M., J. Wan, …, H. A. Stone. 2011. Multiscale approach to link red blood cell dynamics, shear viscosity, and ATP release. *Proc. Natl. Acad. Sci. USA.* 108:10986–10991.
47. Tran-Son-Tay, R., S. P. Sutera, and P. R. Rao. 1984. Determination of red blood cell membrane viscosity from rheoscopic observations of tank-treading motion. *Biophys. J.* 46:65–72.
48. Kraus, M., W. Wintz, …, R. Lipowsky. 1996. Fluid vesicles in shear flow. *Phys. Rev. Lett.* 77:3685–3688.
49. Matoth, Y., R. Zaizov, and I. Varsano. 1971. Postnatal changes in some red cell parameters. *Acta Paediatr.* 60:317–323.
50. Rashidi, Y., G. Simionato, …, A. Darras. 2023. Red blood cell lingering modulates hematocrit distribution in the microcirculation. *Biophys. J.* 122:1526–1537.
51. Bächer, C., A. Kihm, …, S. Gekle. 2018. Antimargination of microparticles and platelets in the vicinity of branching vessels. *Biophys. J.* 115:411–425.
52. Zhou, Q., J. Fidalgo, …, T. Krüger. 2021. Emergent cell-free layer asymmetry and biased haematocrit partition in a biomimetic vascular network of successive bifurcations. *Soft Matter.* 17:3619–3633.
53. Balogh, P., and P. Bagchi. 2019. The cell-free layer in simulated microvascular networks. *J. Fluid Mech.* 864:768–806.
54. Spieker, C. J., G. Závodszky, …, A. G. Hoekstra. 2021. The effects of micro-vessel curvature induced elongational flows on platelet adhesion. *Ann. Biomed. Eng.* 49:3609–3620.